An Automated Neck Flexibility Tester

David J. Tack, Sorin Siegler, and Moshe Kam*, *Fellow, IEEE*

***Abstract*—We investigate automation and control options for the neck flexibility tester (NFT) (P. McClure *et al.*, 1998), a device originally used to measure the flexibility of the human cervical spine. The motivation is to lay the foundations for design and implementation of investigative devices that would allow studies of mechanical properties of the spine under repetitive dynamic loading. We derive the equations of motion for an automated NFT (ANFT) using a Lagrangian formulation. These equations, which represent a simplified first-order model of the dynamics, are used to simulate the ANFT using the software package *Simulink*. Two control schemes are examined: proportional plus integral plus derivative (PID) control and dynamic inversion. Both are simulated for setpoint and tracking control. It appears that PID control is preferred due to its simplicity of design and relative insensitivity to the dynamic model of the ANFT.**

***Index Terms*—Dynamic inversion, *in vitro* testing, neck flexibilitytester, PID control.**

I. Introduction

WHEN TREATING spine pathosis, there exist several surgical procedures and hardware systems that can be used to stabilize the spine [1]–[3], [6], [10], [20]. Development and assessment of these procedures is assisted by various investigative devices and experimental setups. Most setups quantify the degree of stabilization provided by the surgical techniques [2]–[22]. Typically they consist of a loading system which applies incremental load across the cadaveric spine using weights and pulleys ([8], [16], [17]). The loading system is complemented by a kinematic measuring system which records the displacements of the spine, produced in response to applied loads. If it were to allow true anatomical and real-life motion of a spine, a testing device would have six degrees of freedom (DOFs) and take into account nonlinear load displacements and coupled motions. In practice, the specimen's movements in most testing devices are constrained to less than the full six DOFs.

The quasi-static, noncontinuous nature of many testing devices restricts their application to time invariant mechanical properties of the spine. Consequently, important time dependent properties of spinal surgical stabilization such as *screw pull-out*, *fatigue failure* and *migration of bone grafts*, cannot be studied adequately. However, these properties are observed clinically, as they are created by repetitive cyclic loading which occurs during normal routine activity.

Manuscript received September 26, 2000; revised November 20, 2001. *Asterisk indicates corresponding author.*

D. J. Tack is with Data Fusion Laboratory, Department of Electrical and Computer Engineering, Drexel University, Philadelphia, PA 19104 USA.

S. Siegler is with Department of Mechanical Engineering and Mechanics, Drexel University, Philadelphia, PA 19104 USA.

*M. Kam is with Data Fusion Laboratory, Department of Electrical and Computer Engineering, Drexel University, 3141 Chestnut Street, Philadelphia, PA 19104 USA (e-mail: kam@drexel.edu).

Publisher Item Identifier S 0018-9294(02)02996-8.

The main goal of the present study is to establish the foundations for development of a six-DOF *in vitro* spinal testing device which would allow studies of mechanical properties of the spine under repetitive dynamic loading. The first step in this development was to select a mechanical structure for the tester. For this purpose, we used the structure of the *neck flexibility tester* (NFT) [15], developed for testing *in vitro* the mechanical properties of the cervical spine. This unique system is a six-DOF linkage structure (Fig. 1) configured in accordance with the Grood and Suntay parameters [11]. It allows translation along and rotation about three axes e_1, e_2, and e_3. One axis, e_1, is fixed in one body (such as the base of the cervical spine); the second axis, e_3, is fixed in the second body (such as the head); and the third axis, e_2, is a floating axis, perpendicular to the previous two. This nonserial mechanical linkage structure has a number of important features including decoupling in measuring displacements [11] and decoupling in the loads applied through the linkage to the spine. The second step in the development was to select actuators for applying dynamic, cyclic loads to the cadaveric spine.

In the original NFT, loads were applied manually by an operator. This is obviously not desirable for controlled long-term fatigue studies. One of the purposes of the present study is to foster automation of the process, using six actuators, three rotational and three translational, to actuate each of the DOFs of the device. We refer to our proposed device as the *automated NFT* (ANFT). We develop a mathematical model for the ANFT and then examine two control strategies for its operation.

The NFT: In 1998, McClure *et al.* [15] proposed the NFT, a six-DOF apparatus designed for *in vivo* studies. The NFT characterizes the motion between two rigid bodies in a joint, making use of the parameters that Grood and Suntay used in their seminal paper on clinical description of three-dimensional motions [11]. A drawing of the NFT is shown in Fig. 1. It shows the mechanical linkage which allows six DOFs. These are seen as a translation along and a rotation about each of three axes e_1, e_2, and e_3. Testing is performed by applying manually a cyclical force or torque along one axis at a time. Fig. 1 shows a torque applied manually about the e_1 axis.

The ANFT: The objectives of the ANFT is to test spinal devices under cyclic/fatigue loading, replacing manual operation. We develop a mathematical model for the ANFT and propose two control techniques. They are the well-known *PID controller* [5] and *model inversion*, a nonlinear control technique based on finding the inverse of the controlled plant [18]–[19]. Admittedly, our mathematical model ignores nonlinear effects and coupling and the simplifying assumptions limit the applications of the results. Still, the simplified models provide a first-order approximation to the anticipated behavior and are expected to be the

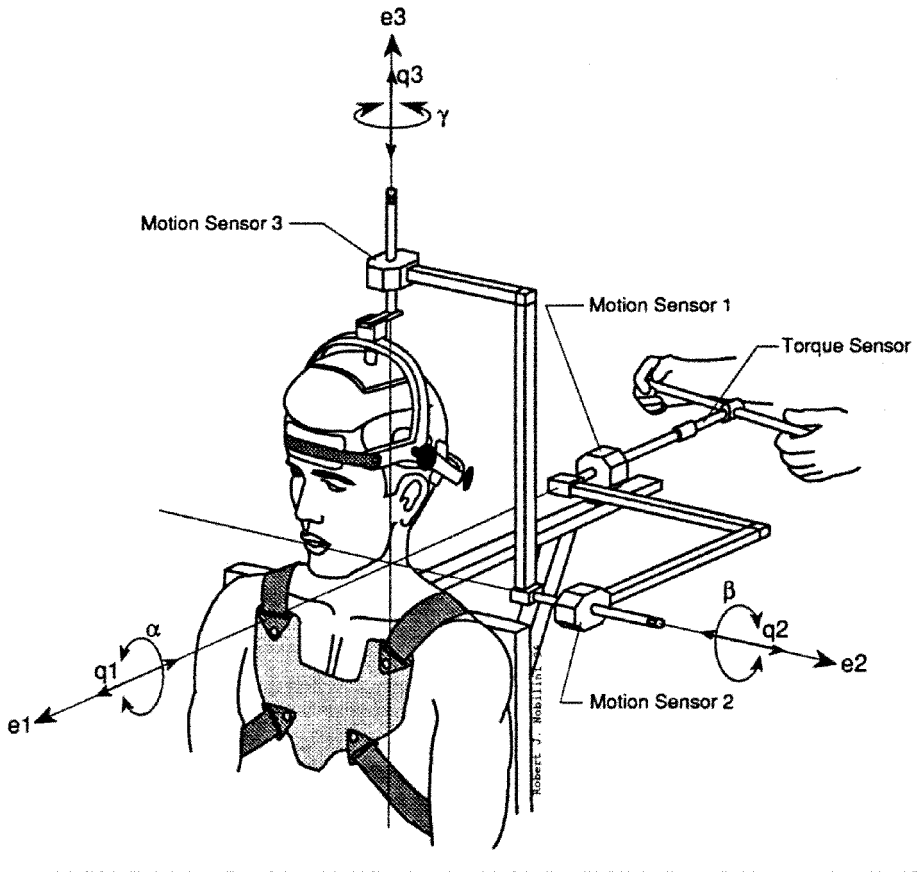

Fig. 1. Schematic drawing of the NFT. It consists of a six-DOF linkage which allows translation and rotation about the axes e_1, e_2, and e_3. It records these motions, as well as the loads applied by the operator. The structure of this linkage is based on the anatomical joint coordinate system defined by [11].

basis on which more complicated and more realistic models can be created (see, also, [7] and [22]).

II. Equations of Motion for the ANFT

A. Development of the Mathematical Model

We develop the equations of motion of the NFT using the *Lagrangian Formulation* with the parameters defined in Fig. 2. The figure shows three joints, each having the ability to translate (r_i) and rotate (θ_i), where $i = 1, 2, 3$. It also shows four centers of mass for the mechanical linkage (labeled a, b, c, and d); these have the respective masses m_a, m_b, m_c, and m_d. Each of these centers of mass has an xyz coordinate reference frame which determines the lengths of each component of the linkages and the relative motion between the centers of mass. Lengths are defined as $l_{j_{kh}}$ where $j = 1, \ldots, 5$, $k =$ a, b, c, and d, and $h = x$, y, and z. For simplicity, $l_{5_{dy}} = l_5$. We denote gravitational acceleration as g and the moments of inertia of each center of mass as I_a, I_b, I_c, and I_d. The *Lagrangian*, L, of the ANFT is given by

$$\begin{aligned} L =& \frac{1}{2m_b}\left(\dot{r}_1^2 + \dot{\theta}_1^2 l_{1_{bx}}^2\right) \\ &+ \frac{1}{2m_c}\left(\dot{r}_2^2 + \left(\dot{r}_1 + \dot{\theta}_2 l_{3_{cy}}\right)^2 + \dot{\theta}_1^2 l_{1_{bx}}^2\right) \\ &+ \frac{1}{2m_d}\left(\dot{r}_2^2 + \left(\dot{r}_3 + \dot{\theta}_1 l_{1_{bx}}\right)^2 + \left(\dot{r}_1 + \dot{\theta}_2 l_{3_{cy}}\right)^2\right) \\ &+ \frac{1}{2I_b}\dot{\theta}_1^2 + \frac{1}{2I_c}\left(\dot{\theta}_2^2 + \dot{\theta}_1^2\right) + \frac{1}{2I_d}\left(\dot{\theta}_2^2 + \dot{\theta}_3^2 + \dot{\theta}_1^2\right) \\ &- g\sin\theta_1\left(l_{1_{bx}}\left(m_b + m_c + m_d\right)\right. \\ &\qquad \left. + \left(l_{2_{bx}} - l_{3_{cx}} + r_2\right)\left(m_c + m_d\right) - l_{4_{cx}} m_d\right) \\ &- g\cos\theta_1\cos\theta_2\left(l_{3_{cy}}\left(m_c + m_d\right)\right. \\ &\qquad \left. + \left(l_{4_{cy}} - r_3 - l_5\right) m_d\right). \end{aligned} \tag{1}$$

We denote the generalized coordinates as $q_i = \{r_1, \theta_1, r_2, \theta_2, r_3, \theta_3\}$; namely, the translations and rotations associated with each joint. The external forces, Q_i, are the net forces acting on each DOF without the effects of gravity or inertia. We include in Q_i the externally applied forces (F_i or τ_i), a frictional element (b_{it} for translation and b_{ir} for rotational friction) associated with the velocity of each DOF and a model of the effect of the attached spine on the linkage. We model the effects of the attached spine as a spring on each DOF (the force that it exerts is k_{it} or k_{ir} multiplied by the displacement from the origin). An actual spine would be more complicated due to coupling between DOFs, but in order to get a computationally tractable approximation we have simplified its response. In future studies we will introduce viscous effects, coupling effects, and nonlinear effects such as material nonlinearity. The specific values and characteristics will be obtained from a quasi-static test performed on the structure prior to dynamic, cyclic testing.

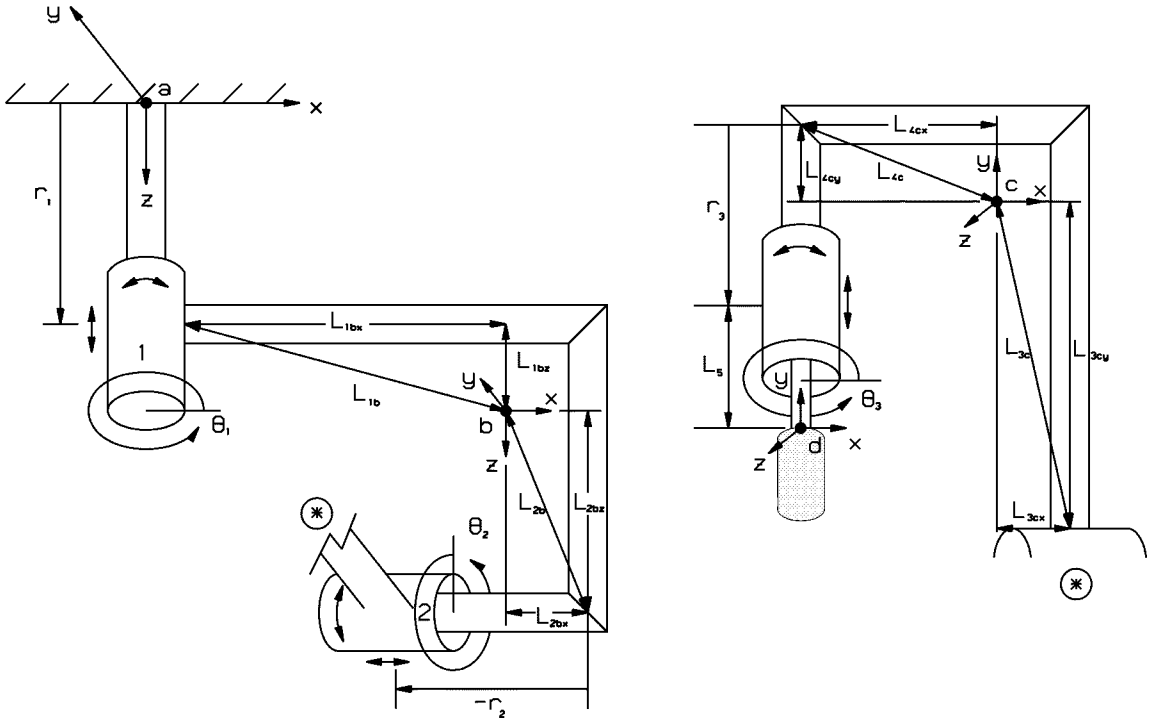

Fig. 2. Parameter definition for the ANFT.

Our present approach results in the following equations which define the motion of the ANFT [see (2)–(7) at the bottom of the page]. We define the states to be

$$x_1 = r_1, \quad x_2 = \dot{r}_1, \quad x_3 = \theta_1, \quad x_4 = \dot{\theta}_1$$
$$x_5 = r_2, \quad x_6 = \dot{r}_2, \quad x_7 = \theta_2, \quad x_8 = \dot{\theta}_2$$
$$x_9 = r_3, \quad x_{10} = \dot{r}_3, \quad x_{11} = \theta_3, \quad x_{12} = \dot{\theta}_3$$

and the inputs as

$$u_1 = F_1, \quad u_2 = \tau_1, \quad u_3 = F_2$$
$$u_4 = \tau_2, \quad u_5 = F_3, \quad u_6 = \tau_3.$$

Our outputs are the positions of each DOF.[1] We solve (2)–(7) for the acceleration of each generalized coordinate and can now write the state space representation of the system

$$\dot{x} = f(x) + Bu$$
$$y = Cx \tag{8}$$

[1]We note that when nonlinearities are added to the model, we need to exercise care concerning possible high velocities in the neutral zone of the spine. This difficuilty can be addressed by adding limiters, or through a more elaborate structure of the controller, possibly by using state feedback.

with

$$f(x) = [f_1 \quad f_2 \quad f_3 \quad f_4 \quad f_5 \quad f_6 \quad f_7 \quad f_8 \quad f_9 \quad f_{10} \quad f_{11} \quad f_{12}]^T$$

where the values of $\{f_i\}_{i=1}^{12}$ are given at the top of the next page, and

$$a_1 = m_b + m_c + m_d$$
$$a_2 = l_{3_{cy}}(m_c + m_d)$$
$$a_3 = m_d l_{1_{bx}}$$
$$a_4 = g\left(l_{1_{bx}} a_1 + (l_{2_{bx}} - l_{3_{cx}})(m_c + m_d) - l_{4_{cx}} m_d\right)$$
$$a_5 = g(a_2 + l_{4_{cy}} m_d + l_5 m_d)$$
$$a_6 = I_b + I_c + I_d$$
$$a_7 = I_c + I_d$$
$$a_8 = m_c + m_d$$
$$a_9 = g m_d$$
$$a_{10} = l_{3_{cy}}^2 a_1 + a_6$$

$$F_1 - b_{1t}\dot{r}_1 - k_{1t} r_1 = \ddot{r}_1 (m_b + m_c + m_d) + \ddot{\theta}_2 l_{3_{cy}} (m_c + m_d) \tag{2}$$

$$\begin{aligned}\tau_1 - b_{1r}\dot{\theta}_1 - k_{1r}\theta_1 =& \ddot{\theta}_1 \left(l_{1_{bx}}^2 (m_b + m_c + m_d) + I_b + I_c + I_d\right) + \ddot{r}_3 m_d l_{1_{bx}} \\ &+ g\cos\theta_1 \left(l_{1_{bx}}(m_b + m_c + m_d) + (l_{2_{bx}} - l_{3_{cx}} + r_2)(m_c + m_d) - l_{4_{cx}} m_d\right) \\ &- g\sin\theta_1 \cos\theta_2 \left(l_{3_{cy}}(m_c + m_d) + \left(l_{4_{cy}} - r_3 - l_5\right) m_d\right)\end{aligned} \tag{3}$$

$$F_2 - b_{2t}\dot{r}_2 - k_{2t} r_2 = \ddot{r}_2 (m_c + m_d) + \sin\theta_1 g (m_c + m_d) \tag{4}$$

$$\begin{aligned}\tau_2 - b_{2r}\dot{\theta}_2 - k_{2r}\theta_2 =& \ddot{r}_1 l_{3_{cy}} (m_c + m_d) + \ddot{\theta}_2 \left(l_{3_{cy}}^2 (m_c + m_d) + I_c + I_d\right) \\ &- g\cos\theta_1 \sin\theta_2 \left(l_{3_{cy}}(m_c + m_d) + \left(l_{4_{cy}} - r_3 - l_5\right) m_d\right)\end{aligned} \tag{5}$$

$$F_3 - b_{3t}\dot{r}_3 - k_{3t} r_3 = \ddot{r}_3 m_d + \ddot{\theta}_1 m_d l_{1_{bx}} - g m_d \cos\theta_1 \cos\theta_2 \quad \text{and} \tag{6}$$

$$\tau_3 - b_{3r}\dot{\theta}_3 - k_{3r}\theta_3 = \ddot{\theta}_3 I_d. \tag{7}$$

$$
\begin{aligned}
f_1 =& x_2 \\
f_2 =& \frac{-1}{a_{15}}\left(b_{1t}x_2 + k_{1t}x_1\right) + \frac{a_2}{a_{15}a_{11}}\left(b_{2r}x_8 + k_{2r}x_7\right) - \frac{a_2}{a_{15}a_{11}}\left(a_5 - a_9x_9\right)\cos x_3 \sin x_7 \\
f_3 =& x_4 \\
f_4 =& \frac{1}{a_{10}a_{17}}\left(-b_{1r}x_4 - k_{1r}x_3 + \frac{a_3}{a_{12}}\left(b_{3t}x_{10} + k_{3t}x_9\right) - \frac{a_3a_9}{a_{12}}\cos x_3 \cos x_7\right) \\
& - \frac{1}{a_{10}a_{17}}\left(\left(a_4 + ga_8x_5\right)\cos x_3 - \left(a_5 - a_9x_9\right)\sin x_3 \cos x_7\right) \\
f_5 =& x_6 \\
f_6 =& \frac{-1}{a_8}\left(b_{2t}x_6 + k_{2t}x_5\right) - g\sin x_3 \\
f_7 =& x_8 \\
f_8 =& \frac{-1}{a_{16}}\left(b_{2r}x_8 + k_{2r}x_7\right) - \frac{a_2}{a_{16}a_1}\left(b_{1t}x_2 + k_{1t}x_1\right) + \frac{a_5 - a_9x_9}{a_{16}}\cos x_3 \sin x_7 \\
f_9 =& x_{10} \\
f_{10} =& \frac{1}{a_{17}}\left(\frac{-1}{a_{12}}\left(b_{3t}x_{10} + k_{3t}x_9\right) + \frac{a_{14}}{a_{10}}\left(b_{1r}x_4 + k_{1r}x_3\right) + g\cos x_3 \cos x_7\right) \\
& + \frac{a_{14}}{a_{10}a_{17}}\left(\left(a_4 + ga_8x_5\right)\cos x_3 - \left(a_5 - a_9x_9\right)\sin x_3 \cos x_7\right) \\
f_{11} =& x_{12} \\
f_{12} =& \frac{-1}{a_{13}}\left(b_{3r}x_{12} + k_{3r}x_{11}\right)
\end{aligned}
$$

$$
\begin{aligned}
a_{11} =& l_{3_{cy}}a_2 + a_7 \\
a_{12} =& m_d \\
a_{13} =& I_d \\
a_{14} =& l_{1_{bx}} \\
a_{15} =& \left(a_1 - \frac{a_2^2}{a_{11}}\right) \\
a_{16} =& \frac{a_{11}}{a_1}a_{15} \\
a_{17} =& 1 - \frac{a_{14}a_3}{a_{10}}.
\end{aligned}
$$

Also, we have

$$
B = \begin{bmatrix}
0 & 0 & 0 & 0 & 0 & 0 \\
\frac{1}{a_{15}} & 0 & 0 & \frac{-a_2}{a_{15}a_{11}} & 0 & 0 \\
0 & 0 & 0 & 0 & 0 & 0 \\
0 & \frac{1}{a_{10}} & 0 & 0 & \frac{-a_3}{a_{10}a_{12}} & 0 \\
0 & 0 & 0 & 0 & 0 & 0 \\
0 & 0 & \frac{1}{a_8} & 0 & 0 & 0 \\
0 & 0 & 0 & 0 & 0 & 0 \\
\frac{-a_2}{a_{16}a_1} & 0 & 0 & \frac{1}{a_{16}} & 0 & 0 \\
0 & 0 & 0 & 0 & 0 & 0 \\
0 & \frac{-a_{14}}{a_{17}a_{10}} & 0 & 0 & \frac{1}{a_{12}a_{17}} & 0 \\
0 & 0 & 0 & 0 & 0 & 0 \\
0 & 0 & 0 & 0 & 0 & \frac{1}{a_{13}}
\end{bmatrix}
$$

and, assuming perfect position sensors on each DOF

$$
C = \begin{bmatrix}
1 & 0 & 0 & 0 & 0 & 0 & 0 & 0 & 0 & 0 & 0 & 0 \\
0 & 0 & 1 & 0 & 0 & 0 & 0 & 0 & 0 & 0 & 0 & 0 \\
0 & 0 & 0 & 0 & 1 & 0 & 0 & 0 & 0 & 0 & 0 & 0 \\
0 & 0 & 0 & 0 & 0 & 0 & 1 & 0 & 0 & 0 & 0 & 0 \\
0 & 0 & 0 & 0 & 0 & 0 & 0 & 0 & 1 & 0 & 0 & 0 \\
0 & 0 & 0 & 0 & 0 & 0 & 0 & 0 & 0 & 0 & 1 & 0
\end{bmatrix}.
$$

A list of our ANFT parameters is given in Table I.

B. Controllability and Observability

Controllability and observability of our model [5], [12] are of obvious interest to the designer of a control system for the NFT. We follow the treatment of nonlinear controllability and observability by Hermann and Krener [12]. Their tests were implemented in *Mathematica*. Using the *Mathematica* commands "Controllability $[f(x), g(x), x]$" and "Observability $[f(x), g(x), h(x), x]$" in *Mathematica*, with the *ProPac* library, we were able to check these properties for our system. We found that the system (8), with the values shown in Table I, is both controllable and observable.

III. PID Control

We simulated a PID controller for the ANFT using *Matlab/Simulink*. The PID controller was tuned for each DOF, using standard techniques (Ziegler–Nichols, Cohen–Coon, and Chien-Hrones-Reswick). A *Simulink* block diagram of the architecture is provided in Fig. 3. The gains shown in Table II provided the best position tracking control for the simulated ANFT with the parameters shown in Table I. We started with no friction or spine model. We used the normalized root-mean-square (RMS) error as the criterion for the accuracy of the ANFT, while it tracks a reference signal. The RMS error between the reference signal and the ANFT output was normalized with respect to the peak-to-peak value of the reference signal by

$$\frac{\sqrt{(y - y_R)^2}}{PtP(y_R)}. \tag{9}$$

Here, y is the output of the ANFT, y_R is the input reference signal and $PtP(y)$ is the peak-to-peak value of y. This measure for error will allow us to consider the tracking error for both rotational and translation reference signals together. We

TABLE I
PARAMETERS OF THE MODEL OF THE ANFT

m_b	34.298 lbm	m_c	32.898 lbm	m_d	4.427 lbm
$l_{1_{bx}}$	10.616 in	$l_{1_{bz}}$	1.654 in	$l_{2_{bx}}$	4.885 in
$l_{2_{bz}}$	7.346 in	$l_{3_{cx}}$	2.307 in	$l_{3_{cy}}$	9.423 in
$l_{4_{cx}}$	8.193 in	$l_{4_{cy}}$	3.539 in	l_5	5.037 in
I_b	4277.2 lbm·in^2	I_c	2956.15 lbm·in^2	I_d	2.213 lbm·in^2
b_{1t}	25000 lbm/s	b_{1r}	100000 lbm·in^2/s	b_{2t}	25000 lbm/s
b_{2r}	100000 lbm·in^2/s	b_{3t}	5000 lbm/s	b_{3r}	1000 lbm·in^2/s
k_{1t}	25000 lbm/s^2	k_{1r}	1000000 lbm·in^2/s^2	k_{2t}	25000 lbm/s^2
k_{2r}	100000 lbm·in^2/s^2	k_{3t}	5000 lbm/s^2	k_{3r}	1000 lbm·in^2/s^2
g	386.09 in/s^2				

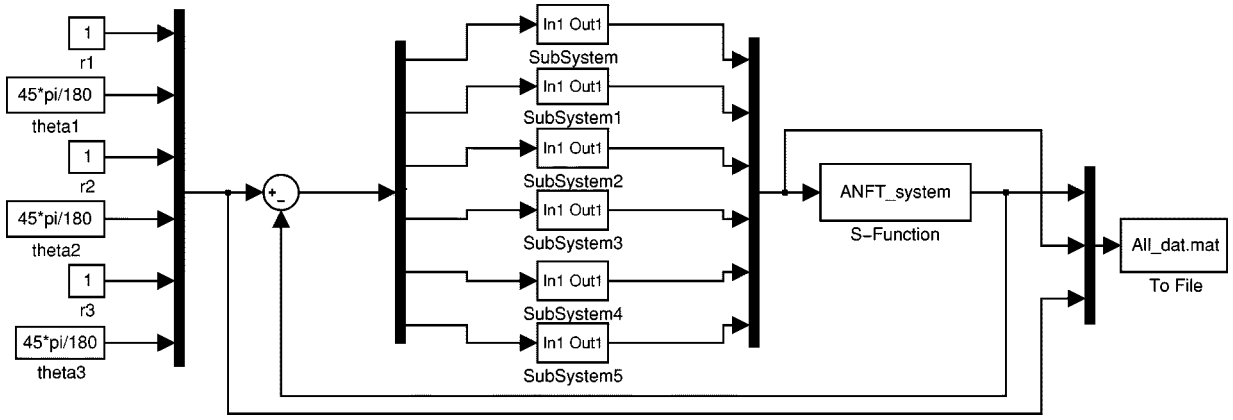

Fig. 3. PID controller for ANFT.

TABLE II
PID GAINS FOR ANFT

PID affecting:	k_p	k_d	k_i
r_1	5250	361725	11.321
θ_1	3375000	1114312.5	424028.3
r_2	600000	120150	134.83
θ_2	3750000	729000	246913.6
r_3	15000	3135	2870.81
θ_3	52.5	2.2125	0.0081356

TABLE III
REFERENCE SIGNALS COMMANDED ALONG EACH DOF

DOF	Reference Signal
r_1	$2sin(2\pi/15)$
θ_1	$45sin(2\pi/30)$
r_2	$2sin(2\pi/15)$
θ_2	$45sin(2\pi/15)$
r_3	$2sin(2\pi/15)$
θ_3	$45sin(2\pi/15)$

TABLE IV
RMS ERRORS FOR THE ANFT TRACKING REFERENCE SIGNALS ALONG ALL DOFS

DOF	RMS Error %
r_1	0.24
θ_1	1.83
r_2	0.32
θ_2	1.13
r_3	0.54
θ_3	0.28
OPI:	0.72

define the overall performance index (OPI) as the average of the RMS tracking error fractions associated with each DOF. For our tracking, an OPI value of less than ten percent RMS error represents acceptable performance.

While the NFT is used to test one DOF at a time, the ANFT can affect several DOFs simultaneously. The PID-controlled ANFT was simulated first with no friction, $k_{ir} = k_{it} = 0$ where $i = 1, 2, 3$. The reference signals along each DOF are provided in Table III (rotations were measured in degrees and translations in inches). We have chosen sinusoidal inputs which would be useful in measuring repetitive loading (at two different frequencies). The RMS error is shown in Table IV. The ANFT tracks the reference signal very closely. Fig. 4 shows the input to the ANFT that was required in order to have the system track the reference signals shown in Table III.

We also tested the PID-controlled ANFT with friction and a spine model. We increased the proportional gains of the PID controllers to those seen in Table V and obtained the OPIs seen in Table VI. Having a tuned PID controller for an ANFT, we were able to simulate an ANFT with the values of parameters seen in Fig. 2. Controllability and observability were maintained even with friction and the spine model.

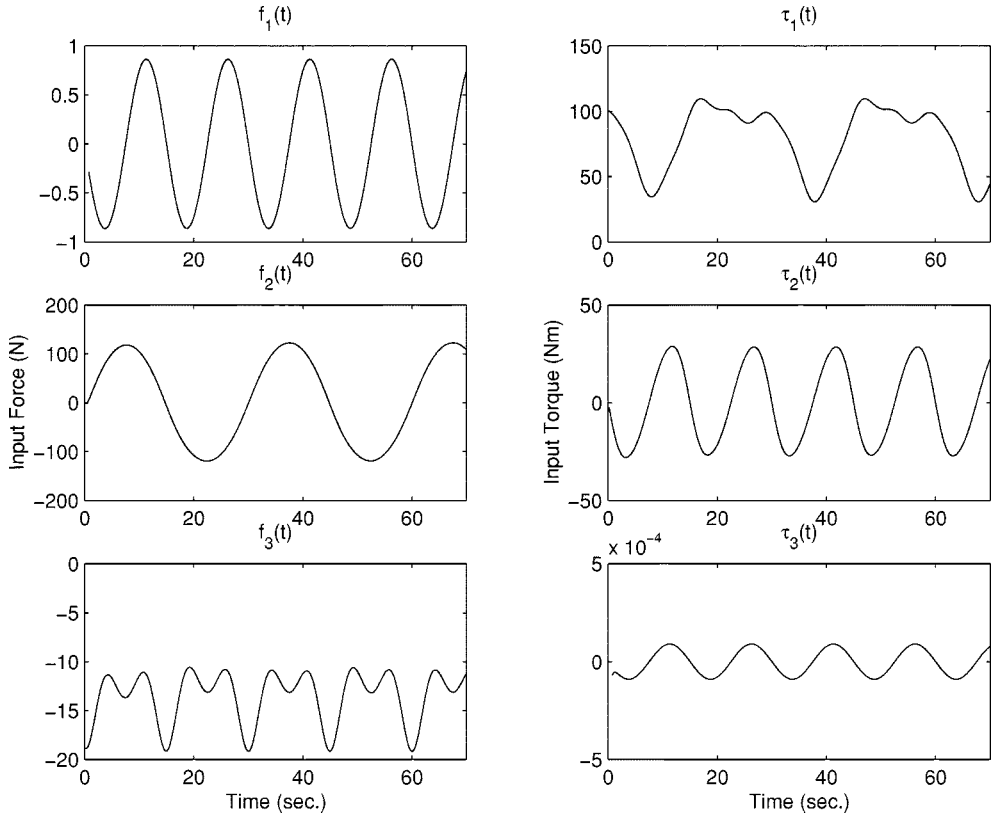

Fig. 4. Input requirements for ANFT.

TABLE V
ADJUSTED PROPORTIONAL GAINS FOR PID CONTROLLED ANFT

PID affecting:	k_p
r_1	525000
θ_1	337500000
r_2	60000000
θ_2	37500000
r_3	1500000
θ_3	5250

TABLE VI
OPIS FOR ANFT

ANFT with	OPI (%)
no friction or spine	0.72
friction and no spine	4.08
friction and spine	8.39

IV. DYNAMIC INVERSION CONTROL

Next, we simulated an ANFT controlled by the nonlinear control technique known as *dynamic inversion* [18], [19]. A *Simulink* block diagram of the technique is shown in Fig. 5. This technique requires an inverse of our nonlinear plant, which can be found through the *Structure Algorithm* of Silverman [18], as generalized for nonlinear systems by Hirschorn [13] and Singh [19]. The *Structure Algorithm* attempts to decouple the states of a nonlinear system to facilitate control. In association with the inverse of the system, we use a *perturbation controller* which takes the form

$$v_i = \gamma_{i0} \int (y_{Ri} - y_i)\, dt + \sum_{j=0}^{n_i-1} p_{ij} \left(y_{Ri}^{(j)} - y_i^{(j)} \right) \quad i = 1, \ldots, r_\alpha \tag{10}$$

where $y^{(j)}$ is the jth derivative of y and r_α is the number of inputs to the original system if the *relative order* [13] of the system is less than infinity; γ_{i0} and p_{ij} are constants. Note that (10) is essentially a state feedback integral controller. In order to maintain stability of the closed loop system, the following polynomials must be Hurwitz

$$\sum_{j=0}^{n_i+1} \gamma_{ij} s^j = 0 \quad i = 1, \ldots, r_\alpha \tag{11}$$

where $\gamma_{ij} = p_{i,j-1}$, $j = 1, \ldots, n_i + 1$. The *relative order* of our system is two. This is a sufficient condition for invertibility and results in the perturbation controller

$$v_i = \gamma_{i0} \int (y_{Ri} - y_i)\, dt + p_{i0} (y_{Ri} - y_i) + p_{i1} \left(y_{Ri}^{(1)} - y_i^{(1)} \right) \tag{12}$$

which is a PID controller. Therefore, the dynamic inversion technique suggests an architecture which contains a PID controller. The major difference between the PID and dynamic inversion controllers is that the latter attempts to generate a feedforward control that commands the ANFT to track a given reference signal based on the inverse of the system. The PID controller uses the reference signals directly and commands the ANFT to track the reference signal.

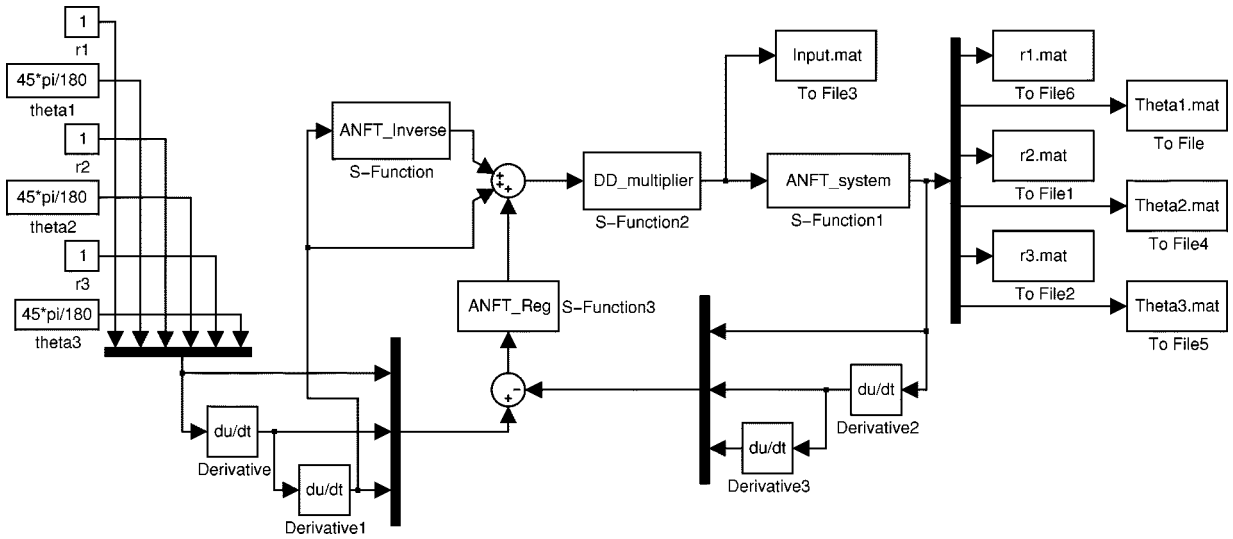

Fig. 5. Dynamic inverse controller for ANFT.

TABLE VII
RMS ERRORS BETWEEN THE INPUT REQUIREMENTS GENERATED BY PID AND THE DYNAMIC INVERSION CONTROLLERS

Input	RMS Error
F_1	1.3018
τ_1	2.5072
F_2	4.0114
τ_2	1.4938
F_3	0.4069
τ_3	0.0001

The gains found for the perturbation controller that resulted in the best tracking were

$$\gamma_{i0} = 5000$$
$$\gamma_{i1} = 7000$$
$$\gamma_{i2} = 2500$$

where

$$i = 1, 2, \ldots, 6. \tag{13}$$

With the system tracking the reference signals in Table III, we obtained an OPI of 3.81% with these gains. We also simulated this system with friction and with both friction and a spine model. As expected, the OPI worsened. Controllability and observability were again maintained. The inputs generated by the Dynamic Inversion controller are very similar to those generated by the PID controller, shown in Fig. 4. These inputs are required to drive the ANFT to track the reference signals shown in Table III. We show the RMS error between these inputs in Table VII.

V. CONCLUSION

Both a PID controller and a dynamic inversion-based controller are viable options for controlling the ANFT in its simplified form. PID controllers have a simple design and are readily available. A PID controller controls the ANFT with a high degree of accuracy (i.e., a low OPI). However, the gains required to control the PID system are higher than the gains required for the corresponding dynamic inversion controller [compare the PID gains in Table II with the dynamic inversion controller gains shown in (13)]. Still, the dynamic inversion based controller is a much more complex system. It uses the inverse of the ANFT mathematical model to generate control signals to command the ANFT to follow a specified trajectory. This process requires that the dynamic model of the ANFT be fairly accurate.

The control signals generated by both control methods were essentially the same. OPI values are also close. This is interesting since the control methods have different approaches and different complexities.

Since the PID controller is much less complex, is relatively independent of a mathematical model of the system and controls the ANFT accurately, it would be prudent to design and build the ANFT with a PID controller. Only if it is found that the higher PID controller gains cause significant noise propagation, would the dynamic inversion based controller become a viable option.

Our results are limited by the first-order nature of the model (linear dynamics, no coupling) and by the modeling of spine effects as a spring attached on each DOF. However, the controllers that we have developed may still find use in practice. There is ample evidence that PID controllers developed for linearized and decoupled models in similar situations were usable in regulation of physical systems by improving parameter tuning [7]. In other cases, designs based on a simplified model were used as the backbone for a more complicated controller (e.g., one that was augmented by a nonlinear compensator [21]).

ACKNOWLEDGMENT

The authors would like to thank Dr. H. Kwatny and B. Reardon for their assistance in this study.

REFERENCES

[1] D. S. Brodke and T. A. Zdeblick, "Modifies Smith-Robinson procedure for anterior cervical discectomy and fusion," *Spine*, vol. 17, no. 105, pp. 5427–5430, 1992.

[2] J. D. Coe, K. E. Warden, C. E. Sutterlin III, and P. C. McAfee, "Biomechanical evaluation of cervical spinial stabilization methods in a human cadaveric model," *Spine*, vol. 14, pp. 1122–1130, 1989.

[3] P. L. Connolly, S. I. Esses, and J. P. Kostuik, "Anterior cervical fusion: Outcome analysis of patients fused with and without anterior cervical plates," *J. Spinal Disorders*, vol. 9, no. 3, pp. 202–206, 1996.
[4] J. J. Crisco III and M. M. Panjabi *et al.*, "Bone graft translation of four upper cervical spine fixation techniques in a cadaveric model," *J. Orthop.*, vol. 9, no. 6, pp. 835–846, 1991.
[5] J. J. D'Azzo and C. H. Houpis, *Linear Control System Analysis and Design: Conventional and Modern*, 4 ed. New York: McGraw Hill, 1995.
[6] M. Deguchi, B. C. Cheng, K. Sato, Y. Matsuyama, and T. A. Zdeblick, "Biomechanical evaluation of translaminar joint fixation. A comparitive study of Poly-L-Lactide pins, screws and pedicle fixation," *Spine*, vol. 23, pp. 1307–1312, 1998.
[7] M. Ferrarin, F. Palazzo, R. Riener, and J. Quintern, "Model -based control of FES-Induced single joint moments," *IEEE Trans. Neural Syst. Rehab. Eng.*, vol. 9, pp. 245–257, Mar. 2001.
[8] V. K. Goel and C. R. Clark *et al.*, "An *in vitro* study of the kinematics of the normal, injured and stabilized cervical spine," *J. Biomech.*, vol. 17, no. 5, pp. 363–376, 1984.
[9] ——, "Evaluvation of effectiveness of a facet wiring technique: An *in vitro* biomechanical investigation," *Ann. Biomed. Eng.*, vol. 17, no. 2, pp. 115–126, 1989.
[10] D. R. Gore and S. B. Sepic, "Anterior cervical fusion for degenerated or protruded discs," *Spine*, vol. 9, no. 7, pp. 667–671, 1984.
[11] E. S. Grood and W. I. Suntay, "A joint coordinate system for the clinical description of Three-Dimensional motions: Applications to the Knee," *ASME Trans. Biomech. Eng.*, vol. 105, pp. 136–144, May 1983.
[12] R. Hermann and A. J. Krener, "Nonlinear controllability and observability," *IEEE Trans. Automat. Contr.*, vol. 22, pp. 728–740, May 1977.
[13] R. M. Hirschorn, "Invertibility of multivariable nonlinear control systems," *IEEE Trans. Automat. Contr.*, vol. 24, pp. 855–865, June 1979.
[14] D. N. Kunz, R. P. McCabe, T. A. Zdeblick, and R. Vanderby Jr., "A multi-degree of freedom system for biomechanical testing," *J. Biomech. Eng.*, vol. 116, pp. 371–373, 1994.
[15] P. McClure, S. Siegler, and R. Nobilini, "Three-dimensional flexibility characteristics of the human cervical spine," *Spine*, vol. 23, no. 2, pp. 216–223, Jan. 1998.
[16] M. M. Panjabi, "Three dimensional testing of the stability of spinal implants," *Orthopade*, vol. 20, no. 2, pp. 106–111, 1991.
[17] M. M. Panjabi and T. Isomi *et al.*, "Looseing at the screw-vertebra junction in multilevel anterior cervical plate constructs," *Spine*, vol. 24, no. 22, pp. 2383–2388, 1999.
[18] L. M. Silverman, "Inversion of multivariable linear systems," *IEEE Trans. Automat. Contr.*, vol. 14, pp. 270–276, Mar. 1969.
[19] S. N. Singh, "Decoupling of invertiable nonlinear systems with state feedback and precompensation," *IEEE Trans. Automat. Contr.*, vol. 25, pp. 1237–1239, June 1980.
[20] A. R. Vaccaro, S. P. Falatyn, and G. J. Scuderi *et al.*, "Early failure of long segment anteror cervical plate fixation," *J. Spinal Disorders*, vol. 11, no. 5, pp. 410–415, 1998.
[21] P. H. Veltnik, H. J. Chizeck, P. E. Crago, and A. El-Bialy, "Nonlinear joint angle control for artificially stimulated muscle," *IEEE Trans. Biomed. Eng.*, vol. 39, pp. 368–380, Apr. 1992.
[22] T. A. Zdeblick, D. Wilson, M. E. Cooke, D. N. Kunz, R. McCabe, M. J. Ulm, and R. Vanderby, "Anterior cervical discectomy and fusion. A comparison of techniques in an animal model," *Spine*, vol. 17, pp. 418–426, 1992.

David J. Tack received both the B.S. and M.S. degrees in electrical engineering from Drexel University, Philadelphia, PA, in 2000 under the supervision of M. Kam.

He is a staff member in the Air Defense Systems Department of the Johns Hopkins University Applied Physics Laboratory, Baltimore, MD. His research interests include robotic and control applications in the medical field and control and guidance of asset defense missiles.

Mr. Tack is the recipient of the 2000 IEEE Philadelphia Section Student Paper Contest First Place award and the 2000 IEEE Region 2 Student Activity Conference Paper Contest First Place award.

Sorin Siegler received the B.Sc. degree in aeronautical engineering from Technion, Israel Institute of Technology, Haifa, Israel, the M.Sc. degree in biomedical engineering from Texas A&M University, College Station, in 1978, and the Ph.D. degree in biomedical engineering from Drexel University, Philadelphia, PA, in 1982.

He is Professor of Mechanical Engineering at Drexel University. His research interests include mechanics of human joints, human motion analysis, and applied dynamics.

Moshe Kam (S'75–M'77–SM'92–F'01) received the B.Sc. degree in electrical engineering from Tel Aviv Univerisity, Tel Aviv, Israel, in 1977 and the M.S. and Ph.D. degrees from Drexel University, Philadelphia, PA, in 1985 and 1987, respectively, under the supervision of P. Kalata.

He is the Robert Quinn Professor of Electrical and Computer Engineering at Drexel University and Director of Drexel's Data Fusion Laboratory. He is also the Director of Drexel's NSA Center for Excellence in Information Assurance Education. His research interests include detection and estimation, data fusion, robot navigation, and pattern recognition.

Dr. Kam is the recipient of a National Science Foundation (NSF) Presidential Young Investigator Award and the C. Holmes MacDonald award for the outstanding young electrical engineering educator. In 2000, he received an IEEE Third Millennium Medal.